Supporting Information

Droplet Jumping: Effects of Droplet Size, Surface Structure, Pinning, and Liquid Properties

Xiao Yan[1,2], Leicheng Zhang[1], Soumyadip Sett[1], Lezhou Feng[1], Chongyan Zhao[2], Zhiyong Huang[2], Hamed Vahabi[3], Arun K. Kota[3,4,5], Feng Chen[2], Nenad Miljkovic[1,6,7,8*]

[1]Department of Mechanical Science and Engineering, University of Illinois at Urbana–Champaign, Urbana, IL, 61801, USA

[2]Institute of Nuclear and New Energy Technology, Tsinghua University, Beijing, 100084, China

[3]Department of Mechanical Engineering, Colorado State University, Fort Collins, CO 80523 USA

[4]School of Biomedical Engineering, Colorado State University, Fort Collins, CO 80523 USA

[5]Department of Chemical Engineering, Colorado State University, Fort Collins, CO 80523 USA

[6]Department of Electrical and Computer Engineering, University of Illinois at Urbana–Champaign, Urbana, IL, 61801, USA

[7]Frederick Seitz Materials Research Laboratory, University of Illinois at Urbana–Champaign, Urbana, Illinois 61801, USA

[8]International Institute for Carbon Neutral Energy Research (WPI-I2CNER), Kyushu University, 744 Moto-oka, Nishi-ku, Fukuoka, 819-0395, Japan

S1. Videos

Video S1. Side-view high-speed microscopy video of coalescence and jumping of binary equally sized water droplets on the superhydrophobic CuO nanostructured surface. Jumping experiments were conducted at an ambient environment temperature $T_a = 25.0 \pm 1.0°C$ and relative humidity $\emptyset = 50 \pm 5\%$. The video was captured at a rate of 7000 frame per second (fps) and displayed at a rate of 5 fps. The radii of the left and right droplets were 290.0 ± 1.0 and 286.5 ± 0.9 μm, respectively.

Video S2. Side-view high-speed microscopy video of coalescence and jumping of binary size mismatched water droplets on the superhydrophobic CuO nanostructured surface. Jumping experiments were conducted at an ambient environment temperature $T_a = 25.0 \pm 1.0°C$ and relative humidity $\emptyset = 50 \pm 5\%$. The video was captured at a rate of 13001 frame per second (fps) and displayed at a rate of 5 fps. The radii of the left and right droplets were 202.0 ± 0.5 and 320.0 ± 1.6 μm, respectively.

Video S3. Side-view high-speed microscopy video of in-plane water droplet jumping on the superhydrophobic hierarchical surface. Jumping experiments were conducted at an ambient environment temperature $T_a = 25.0 \pm 1.0°C$ and relative humidity $\emptyset = 50 \pm 5\%$. The video was captured at a rate of 13001 frame per second (fps) and displayed at a rate of 5 fps. The radii of the left and right droplets were 63.6 ± 1.0 and 59.2 ± 1.5 μm, respectively.

Video S4. Side-view high-speed microscopy video of pinning-mediated droplet rotation on the superhydrophobic CuO nanostructured surface with a pinning line. Jumping experiments were conducted at an ambient environment temperature $T_a = 25.0 \pm 1.0°C$ and relative humidity $\emptyset = 50 \pm 5\%$. The video was captured at a rate of 13001 frame per second (fps) and displayed at a rate of 5 fps. The radii of the left and right droplets were 180.0 ± 1.1 and 186.8 ± 1.9 μm, respectively.

S2. Droplet Jumping Velocity and Direction

To determine the droplet jumping velocity and direction, we traced the droplet centroid trajectory initiating from the detaching point on the surface to the maximum jumping height (Figure S1a). The trajectory was fitted with a parabolic function $y = y(x)$ (Figure S1b), where x and y are the displacement of the droplet in the direction parallel (x axis) and normal (y axis) to the substrate. The displacement in the y axis as a function of time t was fitted with a second order polynomial $y(t)$. A parabolic fit was chosen considering the approximately constant deceleration due to the air drag and gravitational body forces.[1] The jumping direction, quantified by the droplet departing angle θ_j, was obtained via $\tan \theta_j = dy(x)/dx|_{y=y_0}$, where y_0 is the droplet centroid location in the y direction at the detaching point. The direction $\theta_j = 90°$ implies a jumping direction normal the surface plane. The jumping velocity magnitude v_j was determined by taking the derivative of the parabolic curve at the detaching point via $v_j = |\sin \theta_j|^{-1} dy(t)/dt|_{y=y_0}$.
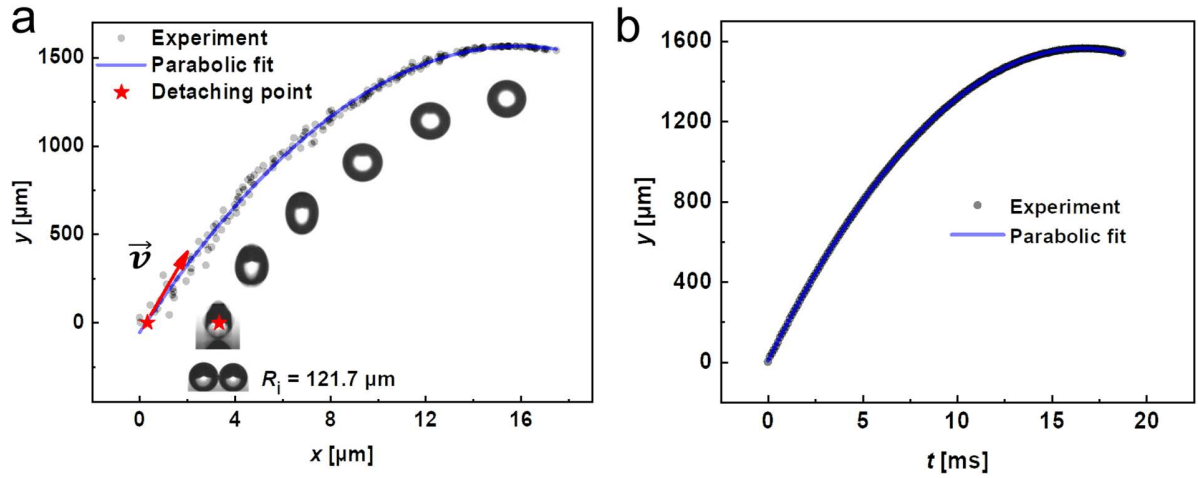

Figure S1. (a) A representative trajectory of the centroid of a jumping droplet. (b) Displacement of the droplet centroid in the y direction as a function of time t. Initial droplet radii were $R_i = 121.7 \pm 3.8$ μm.

S3. Error Analysis

Effects of Injecting Monodisperse Droplets on Droplet Jumping

To quantify the effects of adding monodisperse droplets on target droplet jumping, we first characterized the monodispersed droplet size and velocity approaching the target droplets. Measurements were performed by running the waveform generator at 6.6 - 7.2 V and 10 -500 Hz, covering the parameter range for all jumping experiments. The falling monodisperse droplet trajectories were captured with a high-speed camera (Phantom v711, Vision Research) at a magnification of $\approx$ 25X with a capture rate of 13001 fps. The measured droplet size was R_d = 18.3 ± 1.3 μm, independent on the waveform generator operating conditions. The velocity of the injecting droplets approaching the target droplet was determined from the trajectory of the monodisperse droplets and it was shown that injecting droplet velocity experienced an exponential decay due to the viscous air drag. A representative velocity evolution of the dispensed monodisperse droplet at 7.2 V and 200 Hz and dispensed at a height of $\approx$ 3 mm above the surface was shown in Figure S2. The velocity v_d decreased significantly from $\approx$ 3 m/s to 0.25 m/s until it touched the target large droplet. The average approaching velocity for a working voltage ranging from 6.6 - 7.2 V was 0.12 m/s for the same dispenser-to-surface height.

To analyze the jumping velocity of the droplet pair together with the dispensed injecting droplet, we first consider the instant prior to the coalescence of a target droplet pair with radii R_i. A monodisperse droplet with a radius R_d and injecting velocity v_d approaches the target droplet pair. Upon coalescence between the injecting and target droplets, a slight disturbance of the interface of the target droplet was observed, triggering droplet coalescence between the two target droplets and subsequent jumping. The jumping velocity of the merged droplet (consisted of the droplet pair and the injecting monodisperse droplet) can be estimated via the conversion of energy:

$$\frac{1}{2}\rho V_\mathrm{d} v_\mathrm{d}^2 + \left(A_\mathrm{d} + 2A_\mathrm{i} - A_\mathrm{jd}\right)\gamma\eta \approx \frac{1}{2}\rho V_\mathrm{jd} v_\mathrm{jd}^2 \,, \tag{S1}$$

where V_d and V_jd are the volumes of injecting monodisperse droplet and the merged jumping droplet, respectively. Here, $V_\mathrm{d} = (4\pi/3)R_\mathrm{d}^3$ and $V_\mathrm{jd} = (4\pi/3)R_\mathrm{d}^3 + (8\pi/3)R_\mathrm{i}^3$, ρ and γ are the liquid density and surface tensions, respectively, η is the translational kinetic energy conversion efficiency ($\eta \approx$ 6%).[2-4] Furthermore, A_d, A_i, and A_jd are the surface areas of the monodisperse droplet, target droplet prior to jumping, and jumping droplet, respectively. Here, $A_\mathrm{d} = 4\pi R_\mathrm{d}^2$, $A_\mathrm{i} = 4\pi R_\mathrm{i}^2$, and $A_\mathrm{jd} = 4\pi\left(3V_\mathrm{jd}/4\pi\right)^{2/3}$. Furthermore, v_d and v_jd are the velocity of injecting

monodisperse droplet and jumping droplet, respectively. Note in eq S1 the kinetic energy of the injecting droplet $((1/2)\rho V_d v_d^2)$ was added to the left side without being multiplied by η, allowing a conservative estimate of v_{jd}.

Similarly, for the case where no injecting droplet was involved in the coalescence-induced jumping, the jumping velocity v_j could be solved *via*:

$$(2A_i - A_j)\gamma\eta = \frac{1}{2}\rho V_j v_j^2 , \tag{S2}$$

where $V_j = (8\pi/3)R_i^3$ and $A_j = 4\pi(3V_j/4\pi)^{2/3}$. From eq S1 and S2, we obtain:

$$\frac{v_{jd}}{v_j} = \left[\frac{\frac{1}{2}\rho V_d v_d^2 + (A_d + 2A_i - A_{jd})\gamma\eta}{(2A_i - A_j)\gamma\eta}\frac{V_j}{V_{jd}}\right]^{\frac{1}{2}}, \tag{S3}$$

The addition of monodisperse droplet will add to the size of the jumping droplet. For the droplet jumping with no addition of monodisperse droplets, the conservation of the droplet mass gives rise to:

$$2V_i = V_j , \tag{S4}$$

while for the case involving a monodisperse droplet:

$$V_d + 2V_i = V_{jd} . \tag{S5}$$

From Eqns. S4 and S5, we obtains the ratio of the jumping droplet size with and without considering the monodisperse droplet.

$$\frac{R_{jd}}{R_j} = \left(1 + \frac{R_d^3}{2R_i^3}\right)^{\frac{1}{3}} . \tag{S6}$$

After the coalescence, the detached droplet may also impact the incoming injecting droplets. The time scale of the droplet coalescence is 2.2τ (Figure 7b of the manuscript). The time gap between two adjacent injecting monodisperse droplets is determined by the injecting frequency, $\Delta t = 1/f$. For droplet pairs with radii < 400 μm and maximum injecting frequency f = 500 Hz, $2.2\tau/\Delta t < 1$. Assuming that the droplet pair coalescence is initiated by the addition of the injecting droplet, then the merged droplet detaches from the surface before the following injecting droplet reaches the target droplet. Under this circumstance, conservation of momentum can be applied to the system consisting the detached droplet and injecting droplet:

$$-\rho V_d v_d + \rho V_j v_j \approx \rho V_{jd} v_{jd} , \tag{S7}$$

from which we obtain:

5

$$v_{\mathrm{jd}} = \frac{2R_{\mathrm{i}}^3 v_{\mathrm{j}} - R_{\mathrm{d}}^3 v_{\mathrm{d}}}{2R_{\mathrm{i}}^3 + R_{\mathrm{d}}^3}. \tag{S8}$$

For large droplets with radii ranging from 400 to 800 μm, $1 < 2.2\tau/\Delta t < 3$, implying that more than one droplet will merge into the coalescing droplet pair. However, the total negative momentum induced by the injecting droplets accounts for < 0.01% of the ejecting momentum of the jumping droplet. Therefore, the effects of injecting droplets on jumping velocity of target droplets greater than 400 μm can be safely neglected.

For water droplets at room temperature ($T_{\mathrm{v}} = 25 \pm 1.0°C$) and for the operation conditions of the waveform generator (6.6 - 7.2 V, 10-500 Hz), $R_{\mathrm{d}} = 18.3 \pm 1.3$ μm, $v_{\mathrm{d}} \leq 0.25$ m/s, $\eta \approx 5.6\%$. For an initial droplet radius $R_{\mathrm{i}} \geq 50$ μm, from eq S6 we obtained $(v_{\mathrm{jd}} - v_{\mathrm{j}})/v_{\mathrm{j}} \times 100\% \leq 10.4\%$ and $(R_{\mathrm{jd}} - R_{\mathrm{j}})/R_{\mathrm{j}} \times 100\% \leq 0.8\%$. Furthermore, from eq S8, $(v_{\mathrm{jd}} - v_{\mathrm{j}})/v_{\mathrm{j}} \times 100\% \geq -4.3\%$, confirming that the addition of monodisperse droplets has no significant effects on droplet jumping in our experimental studies, and the droplet dispensing technique can be relied upon for obtaining high-fidelity results for droplet jumping studies.

Similar conclusion can be drawn for the ethanol-water mixtures. For the 20% mass-fraction ethanol water mixture, $\gamma = 38$ mN/m, $\rho = 968.3$ kg/m³, $R_{\mathrm{d}} = 17.7 \pm 1.8$ μm, and $v_{\mathrm{d}} = 0.26$ m/s. For an initial droplet radius $R_{\mathrm{i}} \geq 50$ μm, we obtain $(v_{\mathrm{jd}} - v_{\mathrm{j}})/v_{\mathrm{j}} \times 100\% \leq 10.7\%$ and $(R_{\mathrm{jd}} - R_{\mathrm{j}})/R_{\mathrm{j}} \times 100\% \leq 0.7\%$. From eq S8, $(v_{\mathrm{jd}} - v_{\mathrm{j}})/v_{\mathrm{j}} \times 100\% \geq -4.7\%$.

Given the fact that the jumping direction was almost always perpendicular to superhydrophilic CuO nanoblade surface ($\theta_{\mathrm{j}} = 90 \pm 5°$, Figure 2d in the manuscript), we thus assume that the addition of monodisperse droplets has negligible effect on the jumping direction.
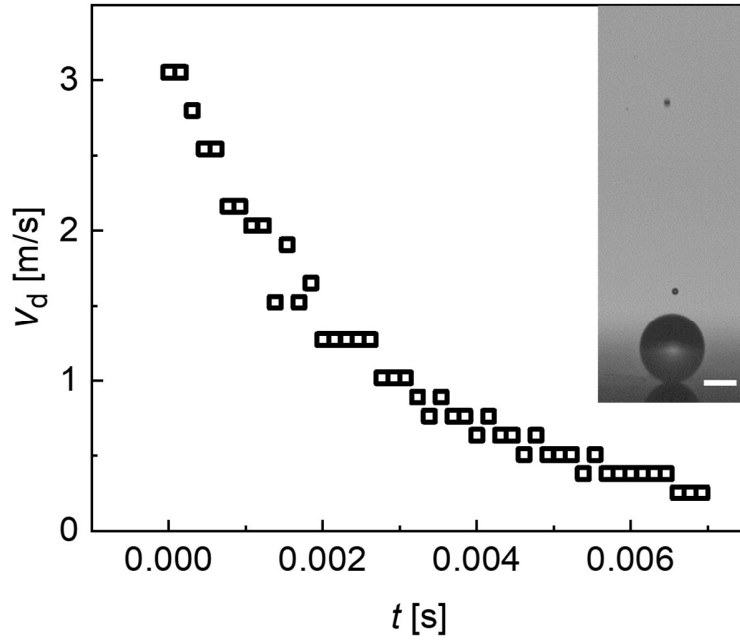
Figure S2. Velocity of the injecting monodisperse droplet approaching the target droplet as a function of time. Inset: High speed optical time snap image of the injecting droplets (two on top) approaching a target droplet (bottom) on a superhydrophobic surface). Scale bar: 100 μm.
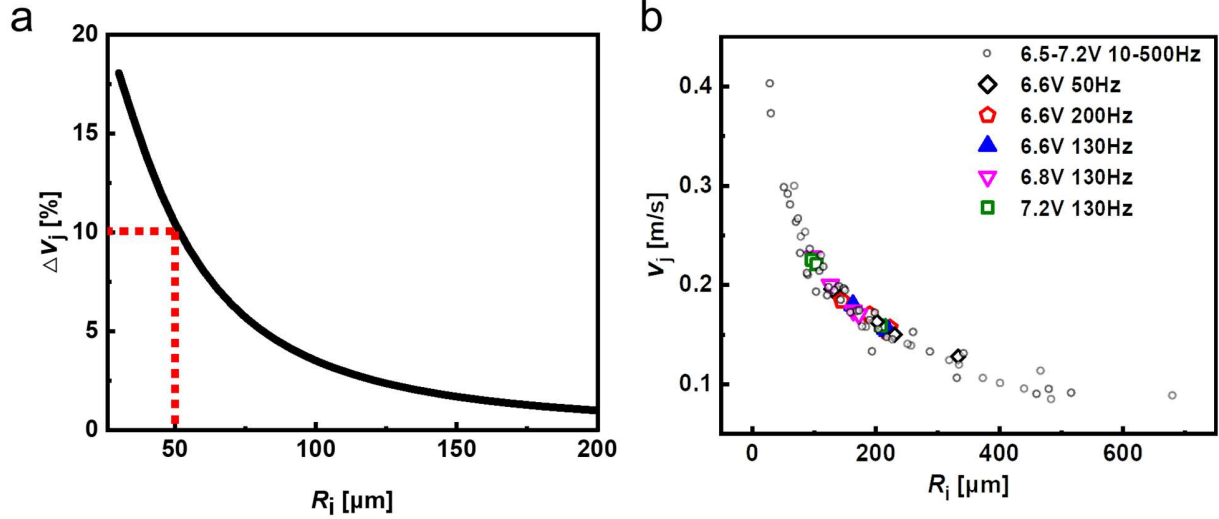

Figure S3. (a) Effects of additional monodisperse droplets on the jumping velocity of the target droplet. Error analysis results show that the jumping velocity difference is within 10% when the initial target droplet radius is over 50 μm, which is the case for the majority (> 95%) of our experiments. (b) Jumping velocity as a function of initial droplet radius at different conditions, which shows that the jumping velocity is independent of the droplet injecting frequency and dispenser working voltage within the current parameter ranges (10-500 Hz and 6.6 - 7.2 V).

Other Sources of Error

In addition to the impact of monodisperse droplets, calibration and data processing was a secondary source of error to the measurement of droplet size and determination of jumping velocity.

We examined the accuracy of calibration by measuring the actual distance of the spacing of a reference micropillar surface (reference distance obtained by scanning electron microscopy), which resulted in uncertainties of 3.1% for the calibration factor.

Due to the high capture rate approaching 13000 fps, the extracted jumping velocity was not sensitive to the detaching frame, which was defined as the frame where the coalesced droplet detaches from the surface. Less than 1.1% variation of the determined jumping velocity was obtained by deviating the detaching frame from the actual detaching frame within ± 2 frames, confirming the reliability of our data processing method.

S4. Jumping of Size-Mismatched Droplets

For two size-mismatched coalescing droplets, the jumping velocity v_j could be analytically predicted by applying eq S2 to the size-mismatched droplets:

$$\frac{1}{2}\rho\frac{4\pi R_j^3}{3}v_j^2 = \left(A_1 + A_2 - A_j\right)\gamma\eta , \tag{S9}$$

$$\frac{4\pi R_j^3}{3} = \frac{4\pi R_1^3}{3} + \frac{4\pi R_2^3}{3} , \tag{S10}$$

where A_1 and A_2 are the surface areas of initial droplets corresponding to radii of R_1 and R_2, respectively. Here, $A_1 = 4\pi R_1^2$ and $A_2 = 4\pi R_2^2$. By solving eq S9 and S10 we obtained:

$$v_j = \sqrt{\frac{6\gamma\eta}{\rho}\frac{\left[R_1^2 + R_2^2 - (R_1^3 + R_2^3)^{2/3}\right]}{R_1^3 + R_2^3}} , \tag{S11}$$

S5. Boundary of Jumping and Non-jumping

We note that no sudden cut-off existed for the jumping velocity of droplets on the superhydrophobic CuO nanoblade surfaces (Figure 2b of manuscript), hence, we took the lowest jumping velocity that could be detected with the visualization and extraction method $v_{\mathrm{j,c}} = 0.05$ m/s as the critical velocity above which jumping occurs based on the limit velocities of large droplets (Figure 2b of manuscript). Substituting $M = (R_2 - R_1)/R_2 \times 100\%$ $(R_2 > R_1)$ into eq S11, then for a given R_1, the critical radius mismatch M_{c} corresponding to $v_{\mathrm{j,c}}$ could be solved via:

$$R_1 = \frac{6\eta\gamma}{\rho v_{\mathrm{j,c}}^2} \frac{1 + (1 - 1/M_{\mathrm{c}})^2 - [1 + (1 - 1/M_{\mathrm{c}})^3]^{\frac{2}{3}}}{1 + (1 - 1/M_{\mathrm{c}})^3}. \tag{S12}$$

Note, in Eq. S12, the contact angle was assumed to approach 180º and the surface-droplet adhesion was neglected.

S6. Wetting Characteristics of Hierarchical Biphilic Surfaces

To confirm the wetting contrast of the hierarchical biphilic CuO nanowire surfaces, we performed atmospheric water vapor condensation experiments in an optical microscope. The experimental details can be found elsewhere.[5] As shown in Figure S4, the condensate droplets on the hilltops and valleys showed distinct morphologies. In the valley regions, the droplets had spherical morphologies (Figure S4a) and showed high mobility after coalescence. On the hilltops, droplets wet the local surface with a low apparent contact angles (Figure S4b) during the initial stage of the droplet growth, showing filmwise condensation.[6]
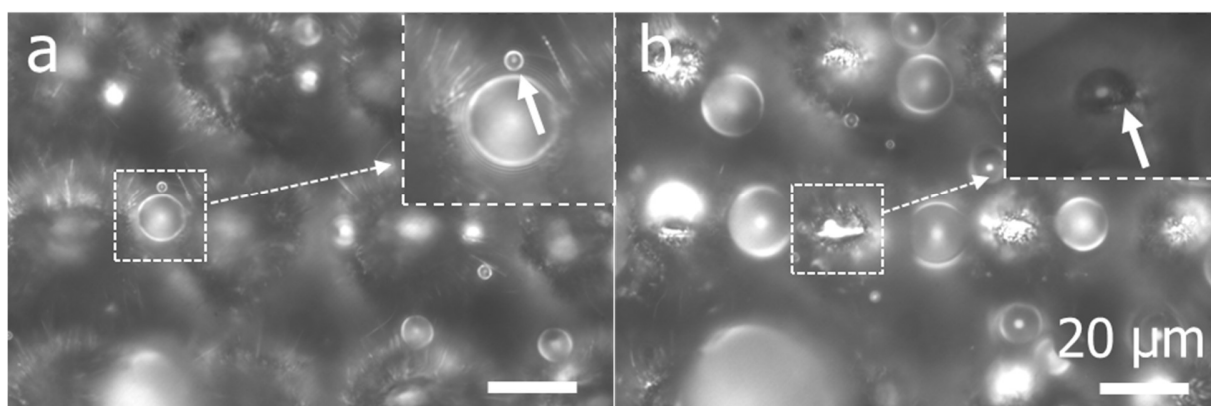

Figure S4. Optical microscopy images of condensation on the hierarchical biphilic CuO nanowire surface, showing the condensate droplet morphologies in the microhill (a) ridge and (b) hilltop areas.

Due to the biphilic features with discrete hydrophilic spots, which tended to pin the three phase contact line and thus confine the base of the droplet, the hierarchical CuO nanowire surfaces show droplet-size-dependent apparent advancing contact angles as the droplets grew due to the addition of monodisperse injecting droplets (Figure S5). The contact angle increased from $\approx 140º$ to $\approx 160º$ as the droplet radius increased from ≈ 50 µm to ≈ 200 µm.
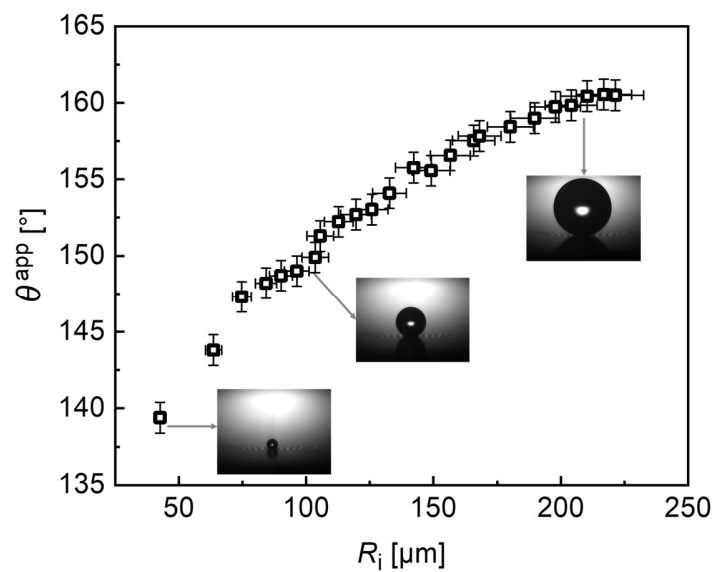
Figure S5. Apparent contact angle (θ^{app}) as a function of droplet radius (R_i) on the hierarchical biphilic surface. Errors of θ^{app} were $\pm 1.0°$, and errors of R_i were $\pm 5\%$.

S7. Determination of Work of Adhesion

To evaluate the work of adhesion of droplets on the hierarchical biphilic surface, we first determined the evolution of the droplet basal area during the growth of the droplet. The droplet basal area, characterized by the droplet base radius $r_{p,k}$ (k = 1, 2, 3…), could be predicted by the geometric pattern of microstructures assuming that the triple-phase contact line remained as a circle as it expanded radially and symmetrically around a fixed center. The location of the center of the expanding contact line circle formed the initial condition which determined the subsequent advancing steps of the droplet base. Three possible initial conditions were considered: center on the hydrophilic hilltops (condition 1, Figure S6a), center in between two adjacent hydrophilic hilltops (condition 2, Figure S6b), and center in between four hydrophilic hilltops (condition 3, Figure S6c). Three advancing paths of the droplet base were solved corresponding to the above initial conditions by gradually enlarging the contact line and judging whether the contact line would be pinned by the hydrophilic hilltop ridges. When the number of the hydrophilic hilltops contacting the contact line at the outer edges was greater than that of the ones that the contact line traversed, then the wetting configuration was regarded as an equilibrium state and the droplet base would not proceed until the droplet contact angle exceeded the apparent advancing contact angle. Thus, an array of equilibrium basal radii ($r_{p,k}$) could be determined with a given initial condition (Table S1). Meanwhile, the solid fraction with respect to microstructures ($\varphi_{m,k}$) defined as total hilltop areas divided by the droplet basal area, could be obtained (Table S1). The solid fraction with respect to nanostructures was estimated via: $\varphi_n = 0.25\pi d^2/l^3 \approx 0.196$, where d ($\approx$150 nm) is the nanowire radius, l ($\approx$300 nm) is the center-to-center spacing of nanowires.
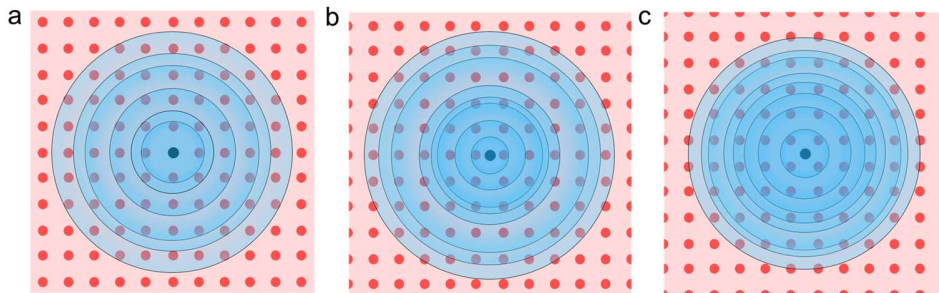

Figure S6. Determination of the equilibrium states of the contact line for three different initial conditions with the droplet base area (light blue) being centered (a) on the hydrophilic hilltops, (b) between two adjacent hilltops, and (c) in between four adjacent hilltops. Hydrophilic hilltops (red circles) were squarely distributed on the superhydrophobic background (light red). The center of the droplet base is depicted by the black circle. For simplicity, the initial conditions corresponding to (a-c) are denoted as condition 1, condition 2, and condition 3, respectively.

Table S1. Arrays of the droplet basal radii and microstructure solid fraction corresponding to different initial conditions.

k	Condition 1		Condition 2		Condition 3	
	$r_{p,k}$	$\varphi_{m,k}$	$r_{p,k}$	$\varphi_{m,k}$	$r_{p,k}$	$\varphi_{m,k}$
1	8.0	1	34.2	0.110	44.2	0.131
2	58.3	0.094	64.0	0.094	86.4	0.103
3	78.3	0.094	109.6	0.085	112.5	0.081
4	118.0	0.097	130.8	0.086	150.8	0.090
5	162.7	0.089	185.8	0.082	180.8	0.088
6	184.1	0.085	204.7	0.086	193.9	0.088
7	214.9	0.085	232.7	0.079	217.7	0.086
8	226.0	0.086			258.6	0.084

The work of adhesion for the coalescing droplets was estimated by:[7]

$$W_a = 2A_p\left[\varphi_{m,k} + (1 - \varphi_{m,k})\varphi_n\right](1 + \cos\theta^{app})\gamma , \tag{S13}$$

where θ^{app} was modeled as a function of droplet radius R_i and pinned base radius $r_{p,k}$:[8]

$$\theta^{app} = \cos^{-1}\left(\frac{r_{p,k}}{R_i}\right) + \frac{\pi}{2} , \tag{S14}$$

The available excessive surface energy[7] was defined as:

$$E_{exc,a} = (2A_i - A_j)\gamma\eta . \tag{S15}$$

The efficiency was assumed to be $\eta = 5.6\%$ according to our previous experiments on the superhydrophobic CuO nanoblade surface.

To evaluate the role of work of adhesion in droplet jumping, we calculated $W_a/E_{exc,a}$ as a function of initial droplet radius R_i (Figure S7). As a demonstration, initial condition 1 (Figure S6a) was considered. For $R_i \leq R_c \approx 90$ μm ($\approx 2L$), $W_a \geq E_{exc,a}$, implying that the available excessive surface energy was not large enough to overcome work of adhesion and jumping was not possible. For $R_i \geq R_m \approx 150$ μm ($\approx 3L$), the work of adhesion contribution is minimized to $\leq$ 21% and droplet jumping was dominated by the inertial-capillary scaling. For $R_c \leq R_i \leq R_m$, work of adhesion accounted for a large proportion of the available excessive surface energy (20%-100%) and droplet jumping velocity was significantly reduced compared to that on the superhydrophobic surfaces where work of adhesion is negligible.

Note that in Eq. S13, the apparent contact angle θ^{app}, rather than the receding contact angle $\theta_{\mathrm{r}}^{\mathrm{app}}$ was used in the work of adhesion. Actually, we found the use of $\theta_{\mathrm{r}}^{\mathrm{app}}$ to underpredict v_{j} by $\approx 20\%$ due to the overestimated work of adhesion in the large droplet radii range, in spite of the good agreement with the experiments in the small radii range (Figure S8).
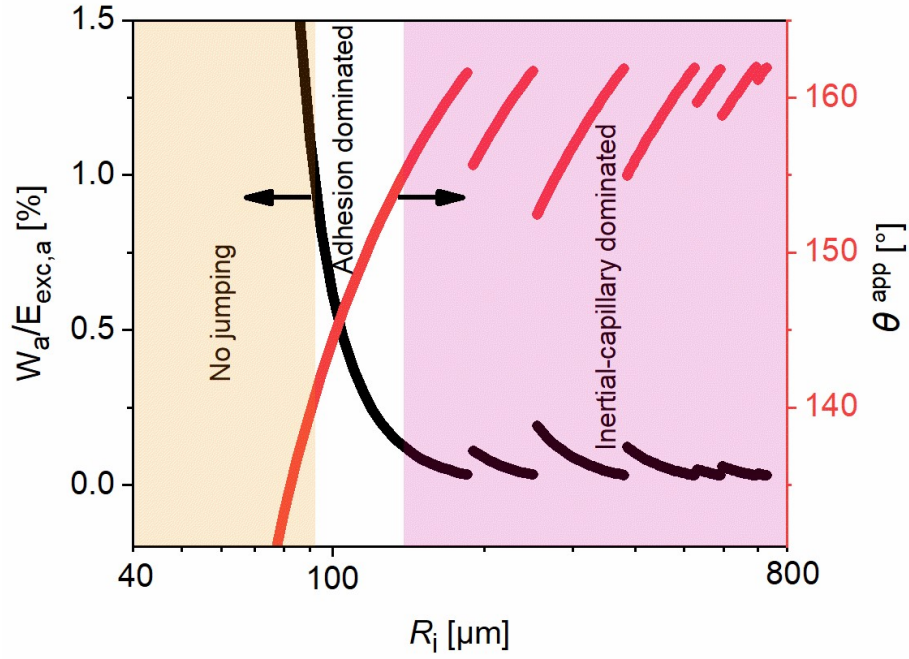
Figure S7. Ratio of work of adhesion to the available excess surface energy $W_a/E_{exc,a}$ and droplet apparent contact angle θ^{app} as a function of droplet initial radii R_i on the hierarchical biphilic surface. Three regions were identified according to the weight of work of adhesion: non-jumping, work-of-adhesion-dominated, and inertial-capillary-dominated regions.
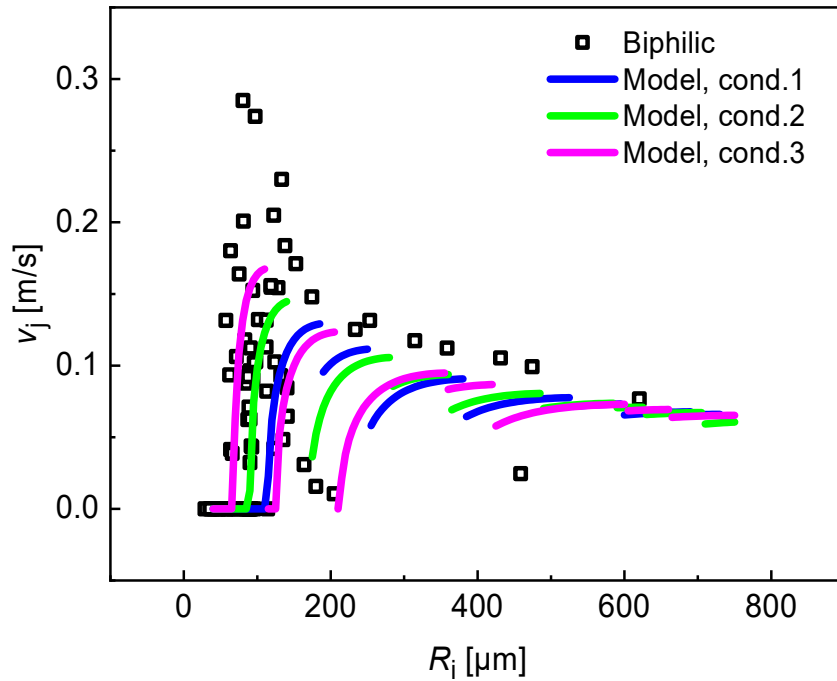

Figure S8. Jumping velocity on the hierarchical biphilic surface predicted using receding contact angle θ_r^{app} ($\approx 120°$) in the work of adhesion term.

16

S8. Translational Kinetic Energy Conversion Efficiency

To determine the translational kinetic energy conversion efficiency of binary equally sized droplets, we took into account the apparent contact angle θ^{app} while calculating the surface areas A_i and volumes V_i of the initial droplets as spherical caps:

$$A_i = 2\pi R_i^2 (1 - \cos\theta^{\text{app}}), \tag{S16}$$

$$V_i = \frac{1}{3}\pi R_i^3 (\cos\theta^{\text{app}} - 1)^2 (\cos\theta^{\text{app}} + 2). \tag{S17}$$

The volume V_j, radius R_j, and surface area A_j of the jumping droplet were determined by:

$$V_j = 2V_i, \tag{S18}$$

$$R_j = \left(\frac{3V_j}{4\pi}\right)^{\frac{1}{3}}, \tag{S19}$$

$$A_j = 4\pi R_j^2. \tag{S20}$$

Substituting eq S16 - S21 into eq S2, we obtained:

$$\eta = \frac{\left(\frac{v_j}{U}\right)^2}{12} \frac{(\cos\theta^{\text{app}} - 1)^2 (\cos\theta^{\text{app}} + 2)}{\left\{1 - \cos\theta^{\text{app}} - [0.5(\cos\theta^{\text{app}} - 1)^2 (\cos\theta^{\text{app}} + 2)]^{\frac{2}{3}}\right\}}, \tag{S21}$$

where v_j/U is the dimensionless velocity and $U = \sqrt{\gamma/\rho R_i}$.

S9. Modelling Jumping Direction

To quantify the role of surface structures on droplet jumping direction, we developed a toy model to relate the jumping angle to the surface structure length scale. To simplify our analysis, we consider a surface with hemispherical structures having characteristic radii R_p and center-to-center spacing s_m shown in Figure S9a, b. Based on experimental observations on the microstructured surfaces (Figure 4d-f of the manuscript), we assumed that jumping direction is perpendicular to the local surface at the liquid bridge contact point (red dot in Figure S9a,b). Depending on the specific location of the droplet pair, the location of the bridge contact point varies, resulting in varying jumping direction. When the droplet radii R_i are relatively small ($R_i < (s_m/2)-R_p$), the droplet could be landing in between the microstructures (Figure S9a). In this case, the size of the structures plays an important role in jumping angle. For a droplet comparable in size with the gap between microstructures ($R_i > (s_m/2)-R_p$), the droplet will form between microstructures, resulting in a lower height of the droplet when compared to the droplet residing on top of microstructures, as depicted in Figure S9b. The jumping angle for the droplet pair could be determined by the geometrical features of the microstructures and droplets:

$$\begin{cases} \theta_j = \theta_p + \theta_h, & R_i < s_m/2 - R_p \\ \theta_j = \theta_p + \theta_s, & R_i \geq s_m/2 - R_p \end{cases} \tag{S22}$$

where $\theta_p = \sin^{-1}[R_p/(R_p + R_i)]$, $\theta_h = \sin^{-1}[(R_p - R_i)/(R_p + R_i)]$, and $\theta_s = \cos^{-1}(s_m/[2(R_p + R_i)])$. From Figure 4a in the manuscript, R_p and s_m were ≈ 55 μm and ≈ 300 μm, respectively. The model results are shown in Figure S9c. As the droplet size increases, the jumping angle converges to 90° (normal to the surface), confirming the limited role of microstructures on jumping angular deflection for large droplets, consistent with experimental observations (Figure S9c). Note, in Figure S9a, we assume that one of the droplets contacts both the microstructure and the substrate, while the second droplet resides on the microstructure only.
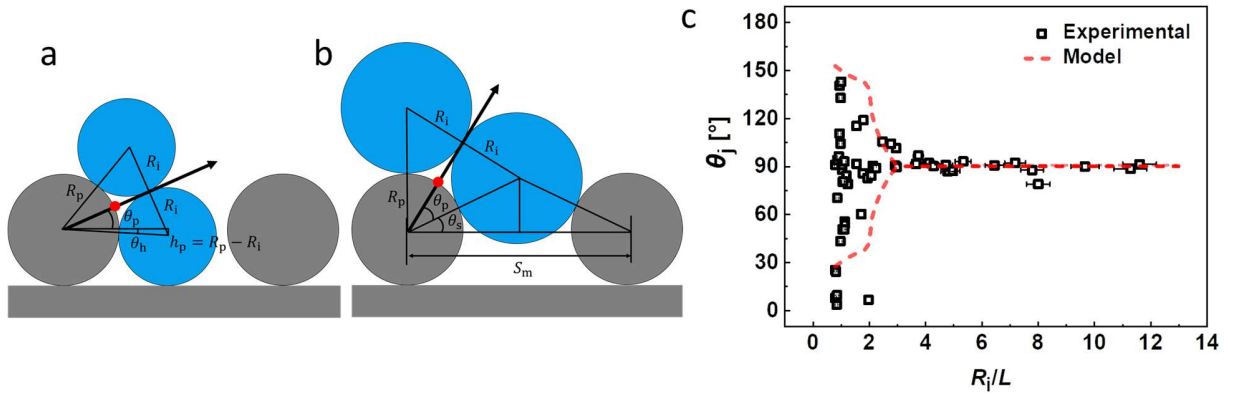
Figure S9. Schematics of droplet coalescence and jumping on hemispherically shaped microstructures having (a) sparse and (b) dense features. (c) Jumping droplet angles in comparison with experimental results. Model parameters: $R_p = 55$ μm, $s_m = 300$ μm. Normal to the surface is $\theta_j = 90°$.

References

1. Liu, F.; Ghigliotti, G.; Feng, J. J.; Chen, C., Self-Propelled Jumping upon Drop Coalescence On Leidenfrost Surfaces. *J. Fluid Mech.* **2014**, 752, 22-38.
2. Enright, R.; Miljkovic, N.; Sprittles, J.; Nolan, K.; Mitchell, R.; Wang, E. N., How Coalescing Droplets Jump. *ACS Nano* **2014**, 8, 10352-10362.
3. Zhang, K.; Liu, F.; Williams, A. J.; Qu, X.; Feng, J. J., Self-Propelled Droplet Removal From Hydrophobic Fiber-Based Coalescers. *Phys. Rev. Lett.* **2015**, 115, 074502.
4. Boreyko, J. B.; Chen, C. H., Self-Propelled Dropwise Condensate On Superhydrophobic Surfaces. *Phys. Rev. Lett.* **2009**, 103, 184501.
5. Chavan, S.; Cha, H.; Orejon, D.; Nawaz, K.; Singla, N.; Yeung, Y. F.; Park, D.; Kang, D. H.; Chang, Y.; Takata, Y.; Miljkovic, N., Heat Transfer through a Condensate Droplet On Hydrophobic and Nanostructured Superhydrophobic Surfaces. *Langmuir* **2016**, 32, 7774-7787.
6. Hou, Y.; Yu, M.; Chen, X.; Wang, Z.; Yao, S., Recurrent Filmwise and Dropwise Condensation On a Beetle Mimetic Surface. *ACS Nano* **2015**, 9, 71-81.
7. Cha, H.; Xu, C.; Sotelo, J.; Chun, J. M.; Yokoyama, Y.; Enright, R.; Miljkovic, N., Coalescence-Induced Nanodroplet Jumping. *Phys. Rev. Fluids* **2016**, 6, 64102.
8. Miljkovic, N.; Enright, R.; Wang, E. N., Modeling and Optimization of Superhydrophobic Condensation. *J. Heat Transfer* **2013**, 11, 111004.